



**AIAA 98-2799**

**Computational Study of Afterbody Effects for  
the Joint Direct Attack Munition (JDAM)**

T. L. Donegan, C. T. Bangasser, and J. H. Fox

Sverdrup Technology, Inc., AEDC Group

Arnold Engineering Development Center

Arnold Air Force Base, Tennessee 37389

19991130 089

**16th Applied Aerodynamics  
Conference**

**June 15-18, 1998 / Albuquerque, NM**

# Computational Study of Afterbody Effects for the Joint Direct Attack Munition (JDAM)\*

*T. L. Donegan, C. T. Bangasser,\*\* and J. H. Fox  
Sverdrup Technology, Inc., AEDC Group  
Arnold Engineering Development Center  
Arnold Air Force Base, TN 37389-6001*

## Abstract

Computational analysis of a JDAM in the  $M_\infty = 0.9$  to 1.4 flow regime determined the effect of changes to the store afterbody and support sting on store loads. The computational results compared well to three sets of wind tunnel data. Accuracy requirements necessitated both that the store geometry be modeled with exceptional detail, and that the Navier-Stokes equations with the Nichols'  $k-\epsilon$  turbulence model be employed. Comparisons to measured data showed excellent agreement with aerodynamic load increments and also with the absolute values of the loads. Analysis using a wall function model for the boundary layer also compared well with data. The comparisons established a sufficient level of confidence in the numerical model as to allow its use in determining the forces and moments free of support effects at the flight Reynolds number.

## Nomenclature

$A_{ref}$  Reference area

$C_A$  Coefficient of axial force  $\left( \frac{F_A}{q_\infty A_{ref}} \right)$

$C_N$  Coefficient of normal force  $\left( \frac{F_N}{q_\infty A_{ref}} \right)$

$C_Y$  Coefficient of side force  $\left( \frac{F_Y}{q_\infty A_{ref}} \right)$

$C_{LL}$  Coefficient of rolling moment  $\left( \frac{M_x}{q_\infty A_{ref}/ref} \right)$

$C_{LM}$  Coefficient of pitching moment  $\left( \frac{M_y}{q_\infty A_{ref}/ref} \right)$

$C_{LN}$  Coefficient of yawing moment  $\left( \frac{M_z}{q_\infty A_{ref}/ref} \right)$

$F_A$  Axial force

$F_N$  Normal force

$F_Y$  Side force

$l_{ref}$  Reference length

$M_x$  Rolling moment

$M_y$  Pitching moment

$M_z$  Yawing moment

$M_\infty$  Free-stream Mach number

$p_\infty$  Free-stream pressure

$q_\infty$  Free-stream dynamic pressure  $(1/2 \rho_\infty V_\infty^2)$

$u_\tau$  Friction velocity

$V_\infty$  Free-stream velocity

$y_n$  Normal distance from wall

$y^+$   $\rho_w y_n u_\tau / \mu_w$

$\alpha$  Angle of attack, deg

$\beta$  Sideslip, deg

$\mu_w$  Viscosity at wall

\* The research reported herein was performed by the Arnold Engineering Development Center (AEDC), Air Force Materiel Command. Work and analysis for this research were performed by personnel of Sverdrup Technology, AEDC Group, technical services contractor for AEDC. Further reproduction is authorized to satisfy needs of the U. S. Government.

\*\* Left Sverdrup Technology in January 1996.

**Approved for public release; distribution unlimited.**

$\rho_w$  Density at wall

$\rho_\infty$  Free-stream density

### Introduction

The harsh environment of the wind tunnel usually requires relatively large sting supports for test articles, often distorting the afterbody shape. Any modification to the afterbody shape affects the expected measured data, necessitating posttest data analysis to quantify the effects of the afterbody changes and of the presence of the sting itself.

Engineers may determine these effects experimentally by performing an incremental investigation using different model support mechanisms such as struts and dummy stings to isolate the sting/afterbody effects. Reference 1 demonstrates this technique. This method, however, assumes linear superposition and requires significant testing and model fabrication, escalating program costs.

Rist<sup>2</sup> established a computational methodology that parallels the experimental approach. He computed the increments for a sting-support interference problem and confirmed that the computed increments compared well with measured increments. Rist concluded that one must accurately model the flow physics in the area of the support geometry and fully define the geometry to correctly determine support effects.

Recently, MDA (McDonnell-Douglas Aerospace) tested its JDAM (Joint Direct Attack Munition) configuration in several wind tunnels with different sting supports and afterbodies. They found that different sting/afterbody geometries were necessary because of the different tunnel hardware arrangements and environments. Because of the disparity in the test results, MDA requested AEDC to computationally investigate the afterbody/sting arrangements and determine the geometric effects in the data. In addition, MDA requested that scale effects from the 1/4-scale model geometry to the full-scale flight vehicle be computed and analyzed as well.

### Experimental Data

Three separate wind tunnel facilities collected measured data for the JDAM. The tunnels included the McDonnell-Douglas Poly-Sonic Wind Tunnel

(PSWT), the Calspan/Buffalo Transonic Tunnel (TST) and the Aerodynamic Wind Tunnel 4T of the Propulsion Wind Tunnel (PWT) Facility at the Arnold Engineering Development Center (AEDC).

The tests gathered aerodynamic load data at free-stream Mach numbers of 0.4 to 1.6 at several angles of attack and sideslip. Unit Reynolds numbers were 1.75 million per foot in 4T and 4.0 million per foot in the PSWT. Computations used 1.75 million per foot for the subscale configurations and 20 million per foot in the full-scale case.

### JDAM Geometry

The JDAM variant for this analysis is a modified Mk-84 bomb with a strapped-on guide bomb kit that converts it to a smart bomb. The kit includes a sectioned plate that conforms to the Mk-84's mid-section surface. Attached to the plate are strakes approximately normal to the external surface. The strap-on kit significantly alters the external geometry, thus requiring wind tunnel testing and analysis to establish the aerodynamic characteristics of the modified configuration. Figure 1 shows the CFD surface model of the JDAM. Modeled with the Mk-84 bomb are the strakes of the strap-on kit, the attachment lugs, and electrical connector.

The analysis required four configurations to be modeled. These configurations are:

Configuration 1: Correct Afterbody, small sting, 1/4 scale (CAS)

Configuration 2: Correct Afterbody, no sting, full-scale, flight Reynolds number (CAN)

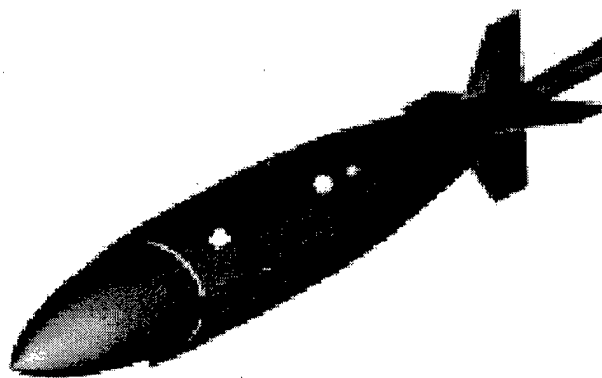


Fig. 1. Overall CFD surface definition; correct afterbody, small string case shown.

Configuration 3: Altered Afterbody, large sting, 1/4 scale, span-matched fins (AAL2)

Configuration 4: Altered Afterbody, large sting, 1/4 scale, area-matched fins (AAL3)

Figures 2 to 5 depict the four afterbody/sting configurations.

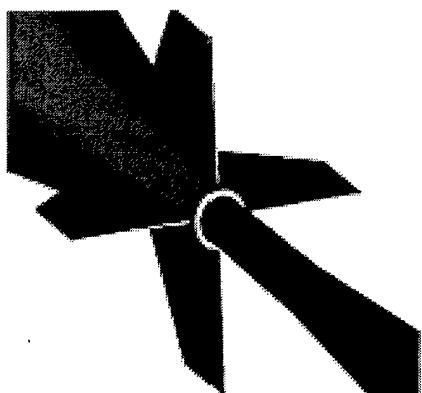


Fig. 2. Aft configuration; correct afterbody, small sting.

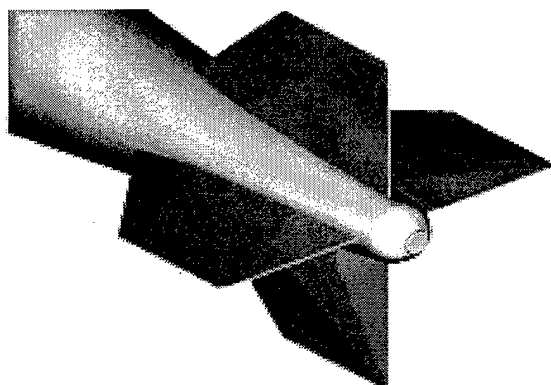


Fig. 3. Aft configuration; correct afterbody, no sting, full scale.

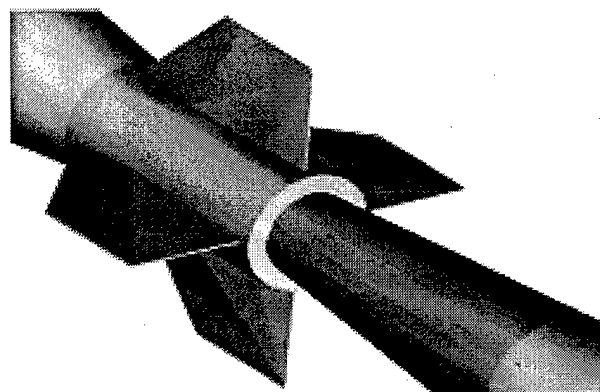


Fig. 4. Aft configuration; altered afterbody, large sting, span matched fins.

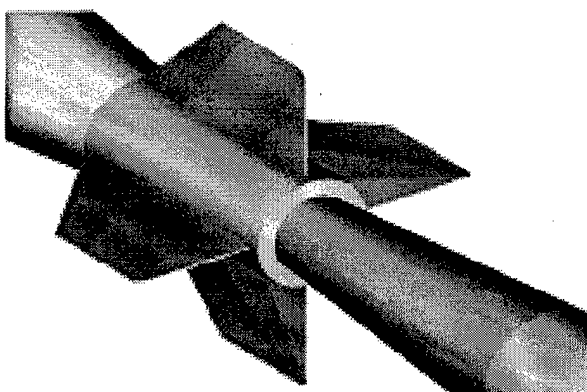


Fig. 5. Aft configuration; altered afterbody, large sting, area matched fins.

All four configurations consist of the Mk-84 body but have dissimilar afterbody/sting/fin regions. The small sting is used during lower dynamic pressure environments, while larger dynamic pressure conditions require the greater support of the large sting. The large sting requires the afterbody to flare out to accept the sting, masking the intersection of the fins and afterbody. The fins may be modeled by either matching the span and assuming the fin/afterbody juncture will be negligible to the loads or by matching the fin area and neglecting the span and length. Configurations 3 and 4 represent these modeling theories.

### Computational Model

The geometric complexity of the JDAM model and the necessity of computing increments for several similar configurations required the use of the chimera overset mesh methodology.<sup>3,4</sup> The chimera methodology allows splitting of the computational domain into smaller subdomains about which body-fitted meshes can be easily generated, thereby simplifying mesh generation for complex geometries. Trilinear interpolation of flow-field information updates the boundary points of each subdomain.

The JDAM surface geometry and near field required 42 viscous meshes, and the far field required two inviscid meshes. The 42 meshes contained a total of 2.7 million mesh points for the 1/4-scale model and 3.3 million mesh points for the full-scale model. The thinner boundary layer of the higher Reynolds number flow for flight required the additional points in the full-scale geometry to accurately resolve the near-wall region. All surface meshes required viscous spacing normal to the

solid walls with a dimensionless body-normal distance parameter ( $y^+$ ) range between 3 and 4. Figure 6 shows an example of the viscous spacing, displaying the nose mesh overlap with the body mesh.

The portions of the strake mounting plates that fit to the surface of the body have sharp, exposed edges. A calculation of the approximate boundary-layer thickness (using flat plate theory) revealed the boundary layer to be five times thicker than the height of the plates, indicating the effect of sharp edges was negligible. By filleting the plate edges, the plates were created with significantly fewer mesh points. The access holes and cutouts in the mounting plates were neglected for the same reason. All other strake mounting hardware (for example, straps, latches, etc.) was neglected as well.

The attachment lugs were simplified for the computational model by neglecting the holes and modeling the lugs as solid bodies. Figure 7 shows selected body mesh planes near the lugs to dem-

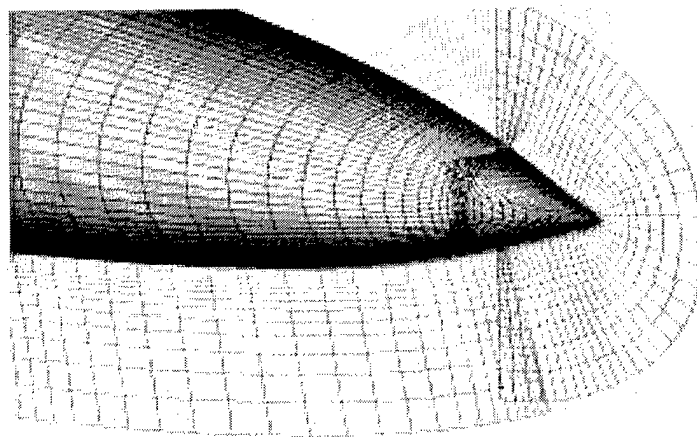


Fig. 6. Sample of grids; nose and forebody.

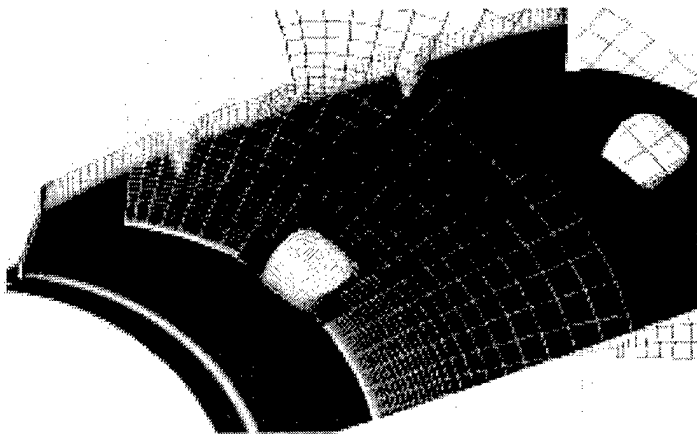


Fig. 7. Sample of grids; strake and lugs.

onstrate the lug surfaces and the computational hole created in the body mesh. The electrical connector was modeled as a cylinder that intersects the body surface. The fins were modeled with a gap between the afterbody surface and the fin roots. The fin pivots, however, were neglected.

### Wall Function Model

Wall function analysis of the JDAM required an additional set of meshes to be assembled to test the recently developed boundary-layer model. The wall function model computes the boundary layer over a surface by relaxing the extremely tight mesh spacing requirement normal to the wall. Using wall functions, the normal wall spacing is set to a  $y^+$  value of 50 to 80, instead of the conventional one to five. The larger spacing allowed the flow solution to converge faster because of larger mesh cells and fewer overall mesh points. The wall function solution was approximately two to four times faster than conventional boundary-layer spacing using the same solution algorithm.

Nichols<sup>5,6</sup> developed the wall function boundary condition to expedite flow solutions for complex geometries. The boundary condition models the inner portion of the boundary layer in conjunction with the  $k-\epsilon$  turbulence model used in this work. Nichols has shown the model to simulate correctly the boundary layer for many problems. In this case, the JDAM was used as an example of a complex geometry at extreme flow conditions as a supplementary test for the model, in addition to giving credence to the remaining solutions in this work.

The wall function analysis for the JDAM consisted of 27 meshes and 2.1 million mesh points and was computed for only one flow condition. Compared to the original meshes, the savings in mesh points and number of meshes are evident.

### Flow Solution

The flow solver was the chimera implementation of a three-dimensional finite difference algorithm used to approximate the solution to the Navier-Stokes and Euler equations. The solver employs the implicit, approximate factorization method of Beam and Warming<sup>7</sup>. Both a Baldwin-Lomax turbu-

lence model<sup>8</sup> and the Nichols' two-equation turbulence model<sup>5,9</sup> are included in the flow solver. Boundary conditions are set explicitly.

All results shown were computed by approximation of the Navier-Stokes equations with Nichols' two-equation turbulence model. The wall function case employs a special boundary condition for the two-equation turbulence model.

## Results

One of the objectives of this effort was the numerical determination of the JDAM aerodynamic performance at flight Reynolds numbers. To establish solution credibility for the JDAM at flight, where no data exist, it was advantageous to predict performance at wind tunnel conditions for which data existed. This required that numerically determined aerodynamic loads of three JDAM subscale models compare well to corresponding wind tunnel data. Also, load differences observed in the measured data due to afterbody alterations should compare well with differences obtained computationally. The quality of these comparisons would provide confi-

dence in the computations, which would then allow the computational analysis of full-scale flight Reynolds number cases.

Table 1 contains a list of CFD solutions computed for the four JDAM configurations. All conditions include the JDAM at a roll angle of -45 deg (clockwise looking upstream from lugs up). Wind tunnel tests previously performed dictated the conditions computed.

The TESS<sup>10</sup> code enables the determination of aerodynamic loads from the CFD solutions. This code allows overlapped meshes that lie on a surface (where pressures may be double-valued) to be rectified with a single unstructured mesh definition, thus yielding a unique pressure value at each surface point. The TESS code integrates the pressures and viscous forces to obtain the load components. Figure 8 defines the force and moment components for the JDAM geometry.

Figures 9 to 11 show comparisons of wind tunnel data from the three tunnels with CFD results for the correct afterbody, small sting configuration

Table 1. Computational Run Matrix.

Run	Mach	Config.*	$\alpha$	$\beta$
1	0.9	1	0	0
2	0.9	1	10	0
3	1.2	1	0	0
4	1.2	1	10	0
5	1.4	1	0	0
6	1.4	1	10	0
7	0.9	3	10	0
8	1.4	3	10	0
9	0.9	4	0	0
10	0.9	4	10	0
11	1.4	4	0	0
12	1.4	4	10	0
13	0.9	1	10	5
14	0.9	4	10	5
15	0.9	2	0	0
16	0.9	2	0	5

\*Configurations

1. Correct Afterbody, small sting, 1/4 scale (CAS)
2. Correct Afterbody, no sting, full-scale, flight Reynolds number (CAN)
3. Altered Afterbody, large sting, 1/4 scale, span-matched fins (AAL2)
4. Altered Afterbody, large sting, 1/4 scale, area-matched fins (AAL3)

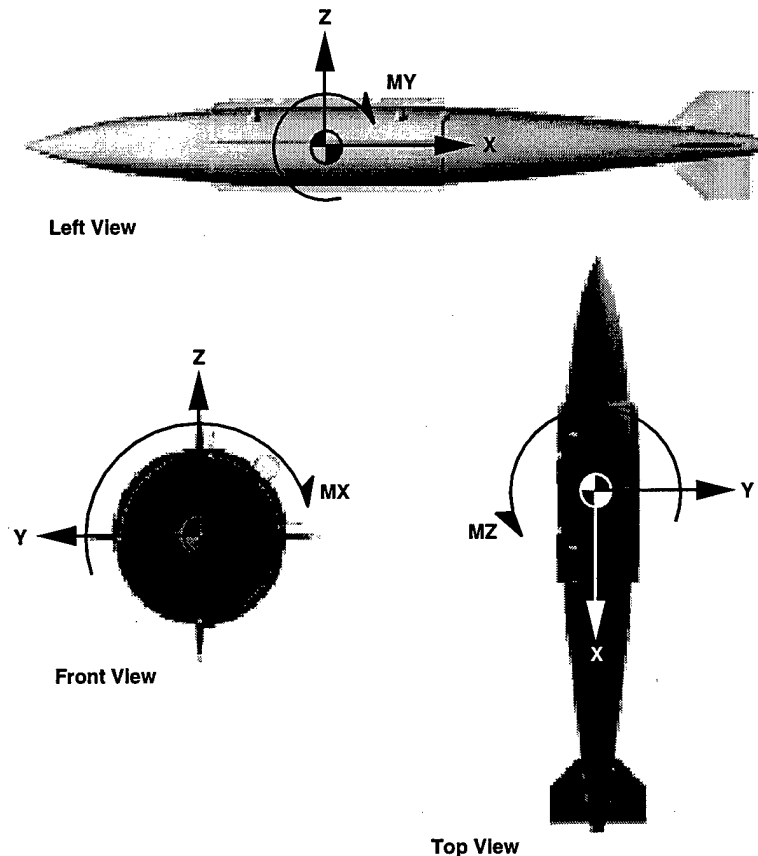


Fig.8. CFD body axis coordinate system.

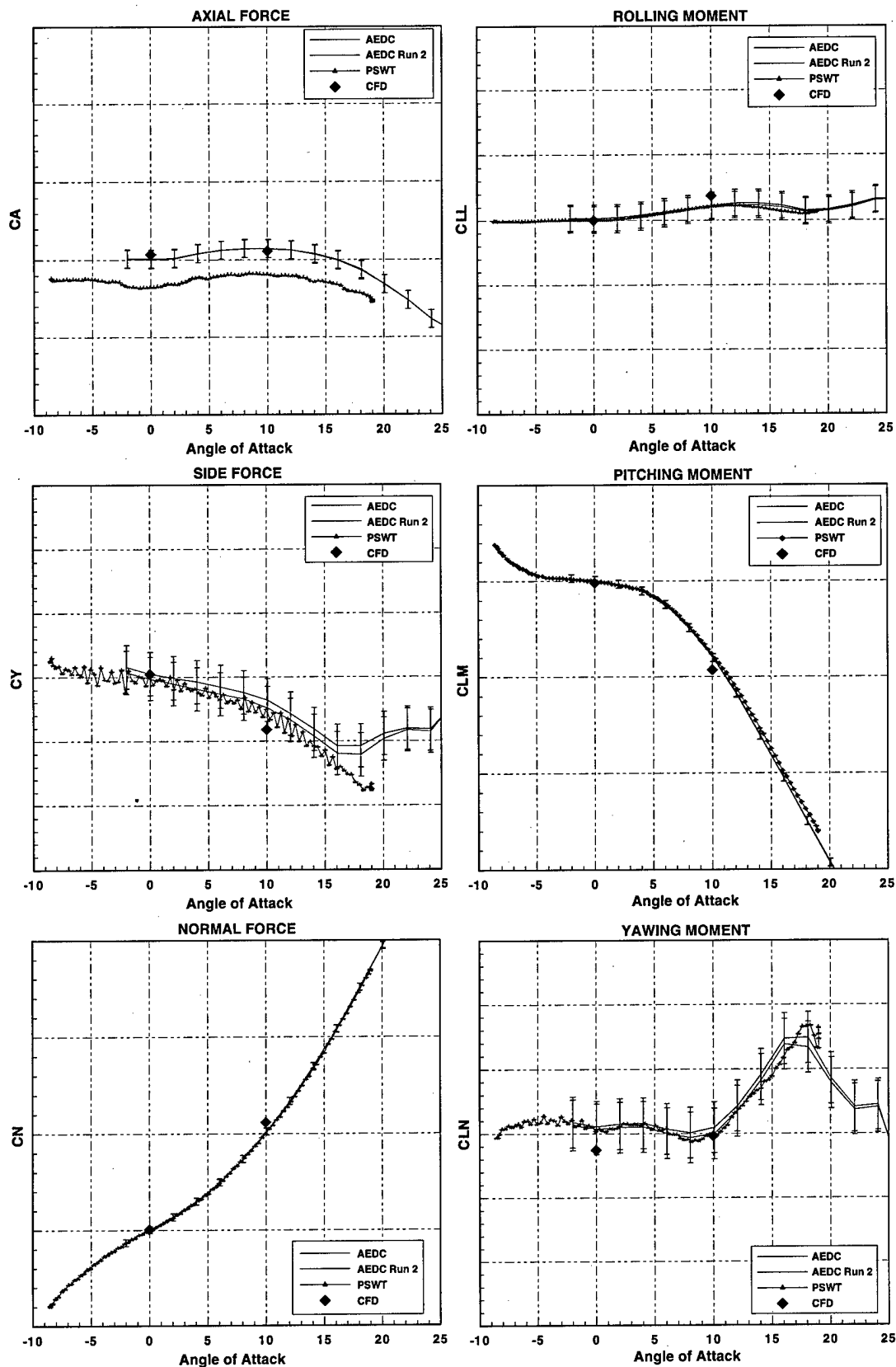


Fig. 9. Correct afterbody; small sting, 0.9 Mach, 0 deg  $\beta$ .

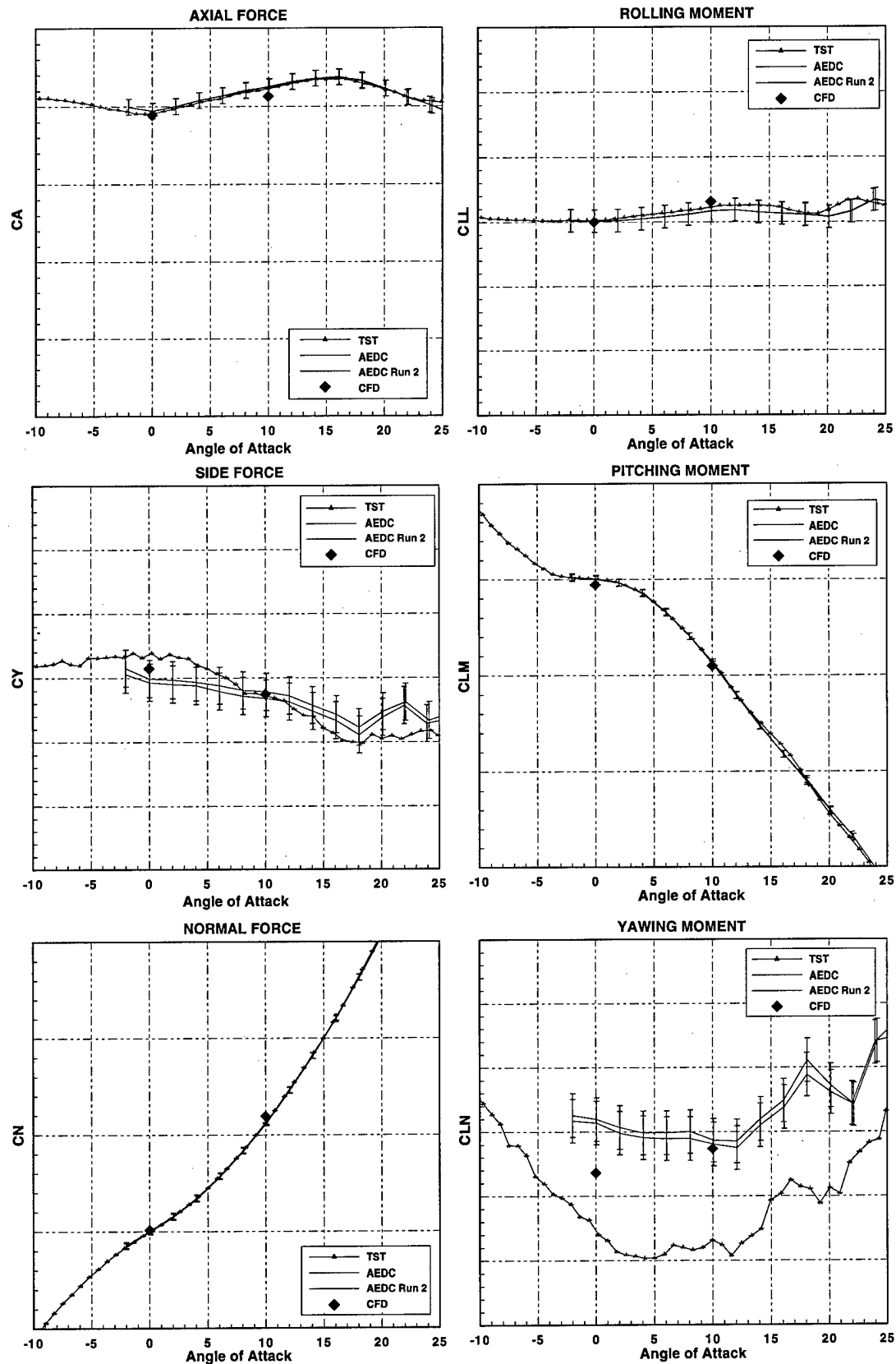


Fig. 10. Correct afterbody; small sting, 1.2 Mach, 0 deg  $\beta$ .



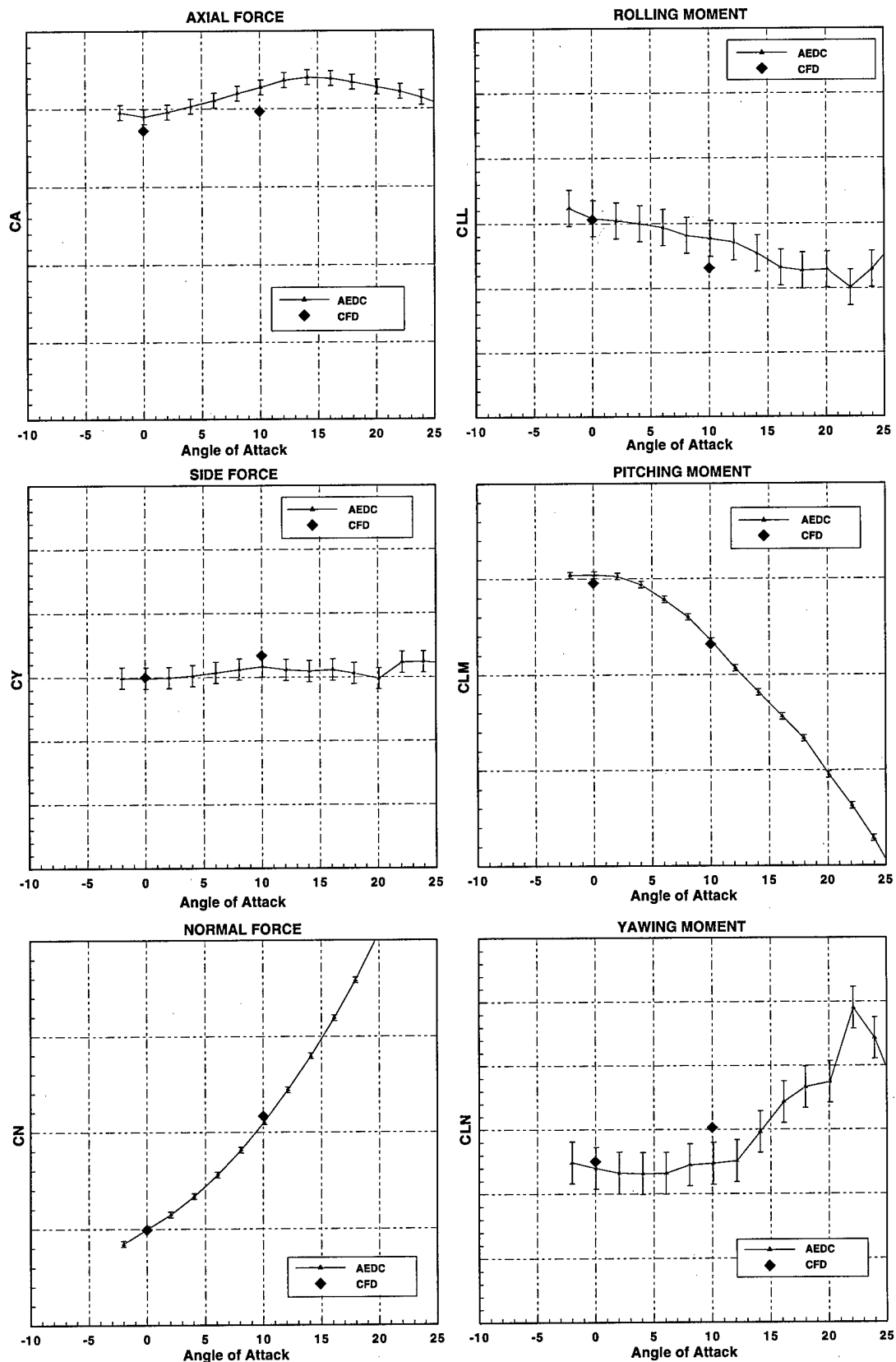


Fig. 11. Correct afterbody, small sting, 1.4 Mach, 0 deg  $\beta$ .

(CAS). The plots show good overall comparison of CFD solutions with data at the three Mach number cases. The primary discrepancies also exist among the measured data. These discrepancies occur primarily because of differences in the Reynolds numbers of the different tunnel tests. The computations adopted the Reynolds number of the 4T test. In most of the comparisons in Figs. 9 and 10, the computed results fall within the uncertainty of the 4T instrumentation. The brackets about the data in the figures denote the uncertainty.

In Figs. 12 and 13, comparisons indicate good agreement between CFD and test data for the altered afterbody, large sting, span-matched fin configuration (AAL2). A comparison of configurations shows that there are no substantial differences between the performance of the AAL2 configuration and that of the CAS configuration (compare Figs. 12 and 13 with Figs. 9 and 11). Significant differences do exist in pitching moment at 10-deg angle of attack between the AAL3 configuration and the CAS configuration (compare Figs. 14 and 15 with Figs. 9 and 11). Although there is a notable difference in the measured pitching moments between the configurations, the computations correctly reflect this difference.

By calculating increments among the three configurations, comparisons are made between experimental and computed increments and shown in Figs. 16 and 17. The computed differences compare very well to the test data differences, especially in the  $M_\infty = 1.4$  cases. However, a comparison of configurations shows, in all instances, the large sting, area-matched configuration (AAL3), exhibits the greatest difference with the correct afterbody (CAS) configuration. This observation indicates the span-matched (AAL2) configuration more closely replicates the correct afterbody. In this span-matched case, the large afterbody flare evidently simulates the boundary-layer displacement found on the actual afterbody while conserving the primary outer fin region. The area-matched configuration (AAL3) has more fin extension exposed to the flow, producing additional moments on the store body.

Figures 18 and 19 show comparisons of data and computations for two configurations (CAS and AAL3) at a yaw angle of 5 degrees and angle of attack of 10 degrees. The comparisons continue to

yield excellent agreement of solutions and data, even with a significant sidewash and total incidence angle.

Also presented in Fig. 18 is the wall function flow solution. The wall function model correctly simulates the boundary layer, even at the relatively high incidence angle. The solution produces comparable results with the data and other presented solutions. The wall function model thus has promise of yielding faster, yet accurate, solutions for complex flows.

Since the excellent comparisons between computations and measured data for all three configurations produce confidence in the computations, the free-stream store solution was computed representing the full-scale geometry. The correct afterbody, no-sting case (CAN) configuration represents the full-scale geometry. Figure 20 shows a comparison of the actual afterbody geometry (CAN) and the correct afterbody, small sting configuration (CAS). Any differences denote the effect of the sting attachment to the store. In this case, very little difference exists except for the axial force. The absence of the sting allows closure of the body and the pressure relief that accompanies it, thus accounting for the axial force difference. This information indicates the small sting has little effect on the store loads at these conditions.

### Concluding Remarks

The aerodynamic flow fields about three subscale JDAM configurations were computed to determine effects of afterbody changes to overall store loads. The computed results were compared to measured data from three different wind tunnels. Overall, the comparisons were excellent, as both the absolute store loads and differences due to the afterbody changes matched the data well. Seventy percent of the computed forces and moments fell within the stated pre-test wind tunnel uncertainties.

The computational results illustrate the present capability at AEDC to reliably predict the performance of complex subscale and full-scale geometries at test and flight Reynolds numbers. The wall function solution for the same configuration additionally gives promise of reliable results with significant savings of computational time.

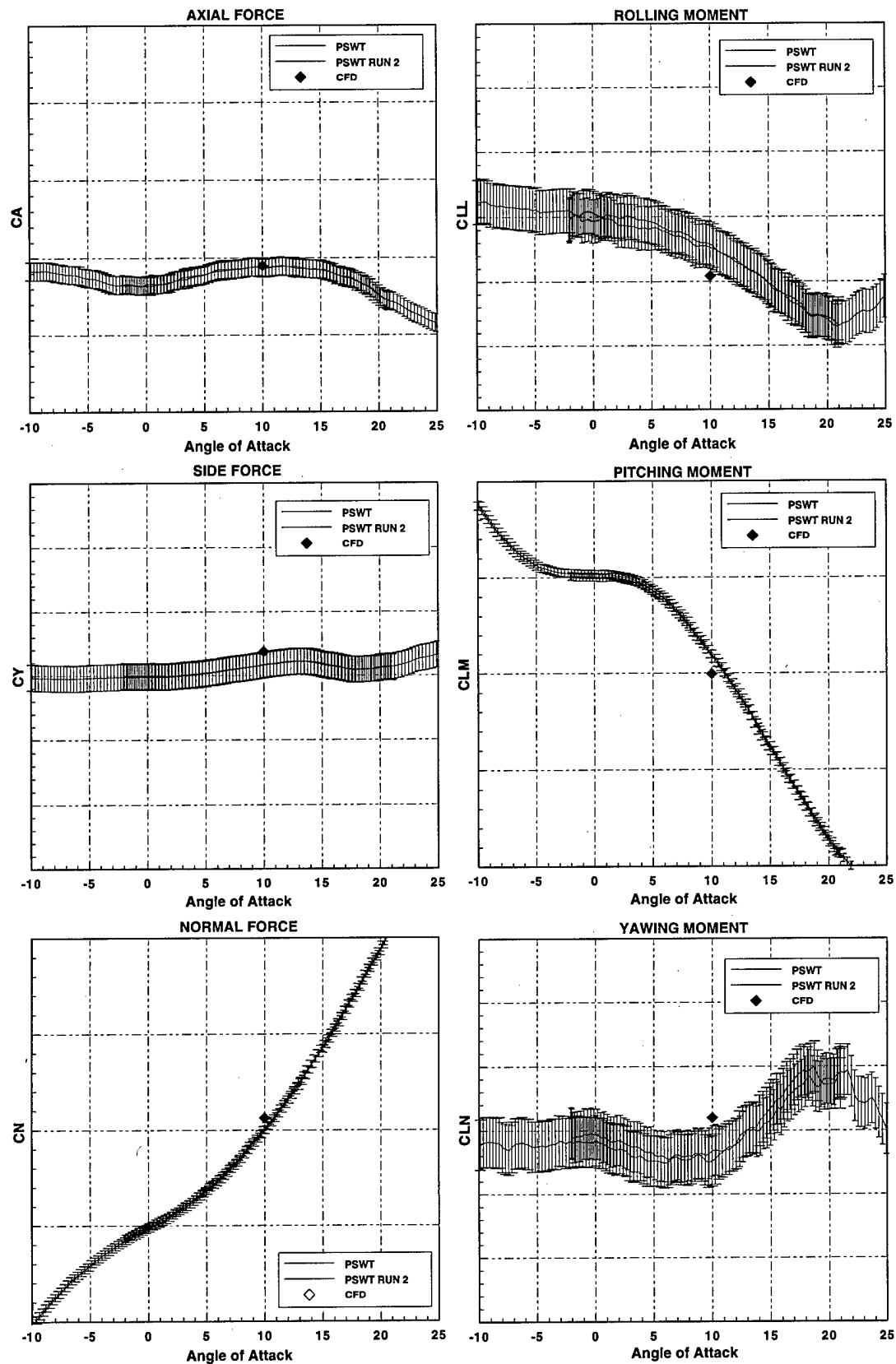


Fig. 12. Altered afterbody, large sting, span-matched fins; 0.9 Mach, 0 deg  $\beta$ .

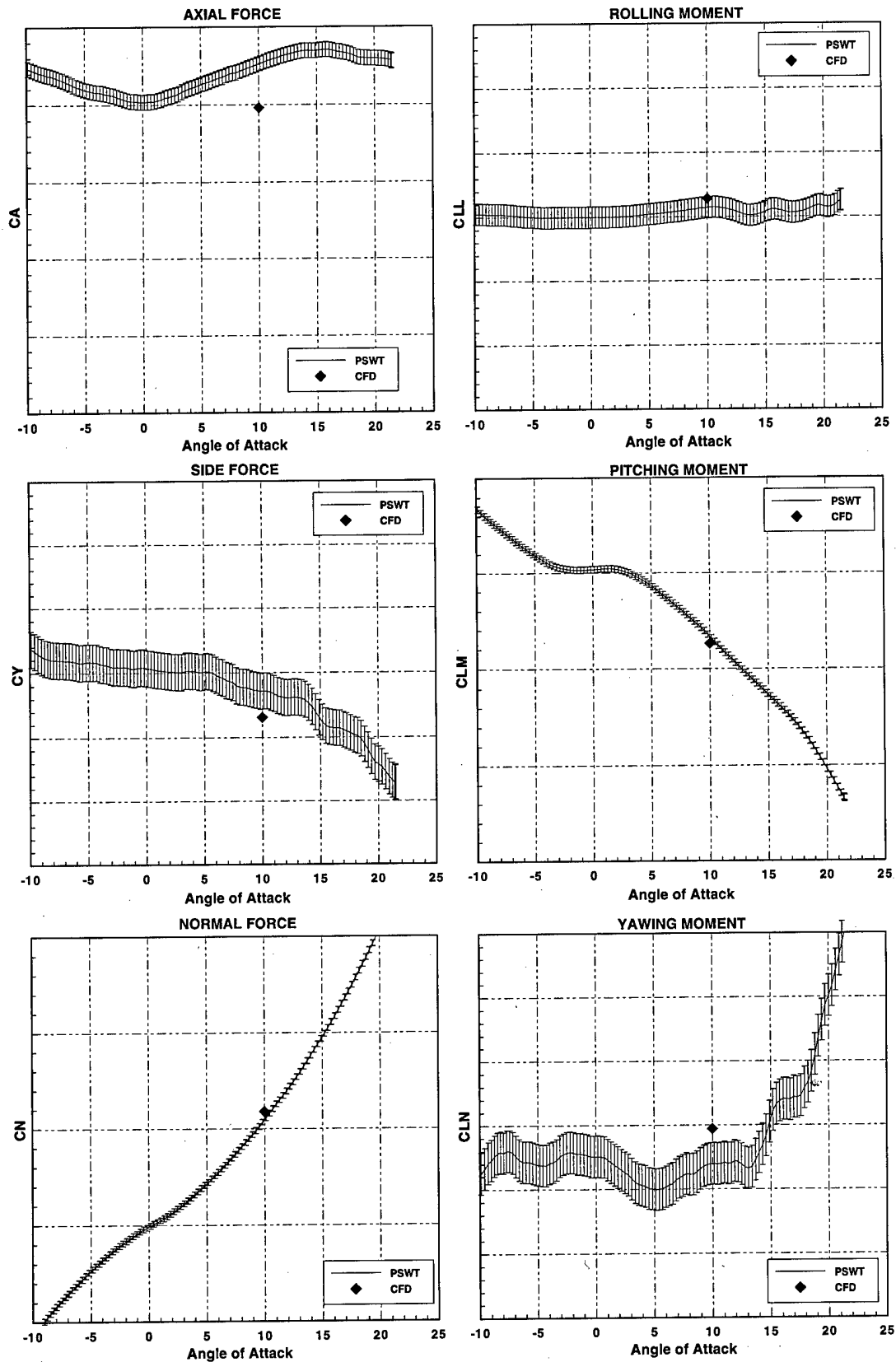


Fig. 13. Altered afterbody, large sting, span-matched fins; 1.4 Mach, 0 deg  $\beta$ .

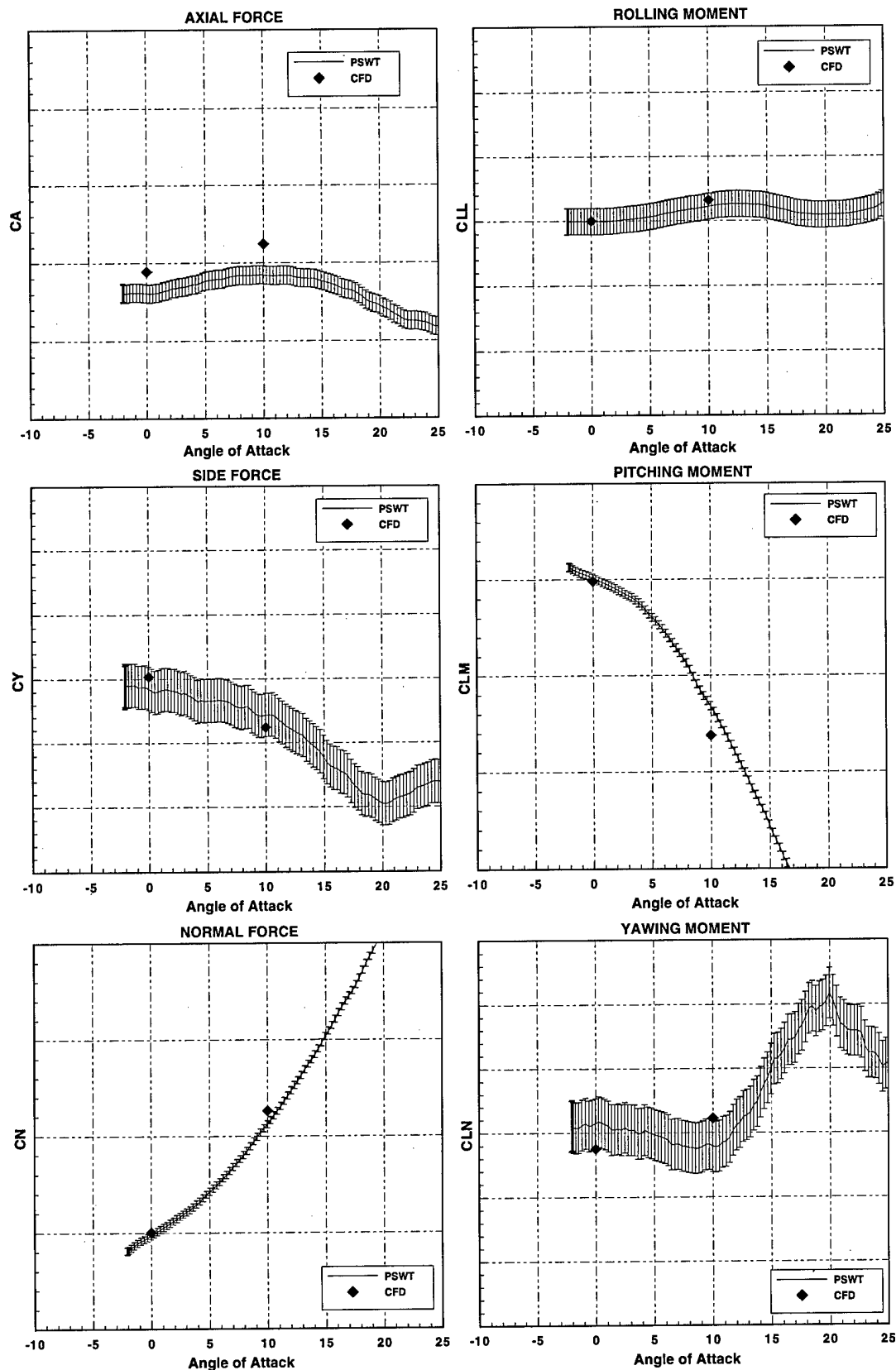


Fig. 14. Altered afterbody, large sting, area-matched fins; 0.9 Mach, 0 deg  $\beta$ .

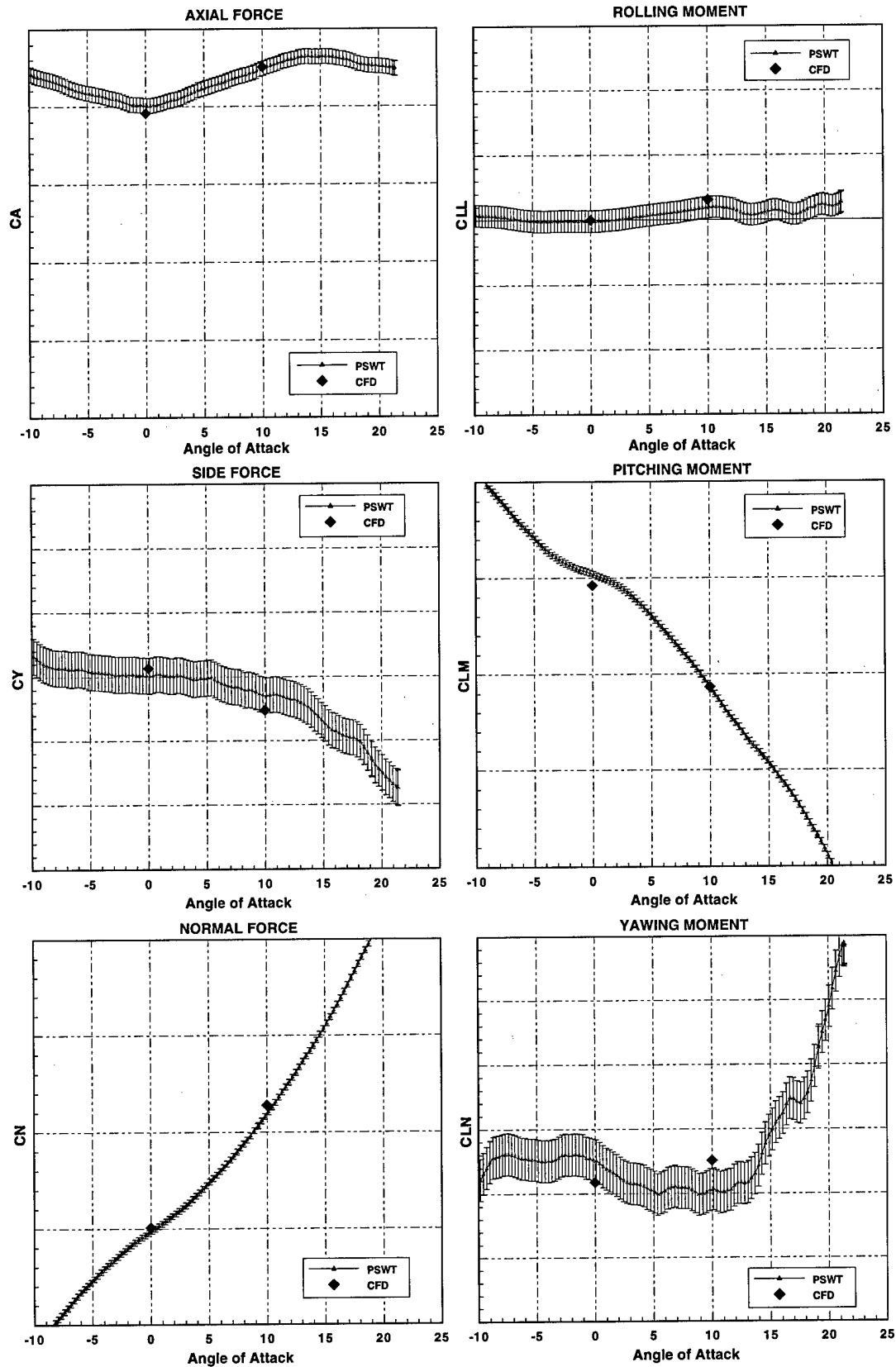


Fig. 15. Altered afterbody, large sting, area-matched fin; 1.4 Mach, 0 deg  $\beta$ .

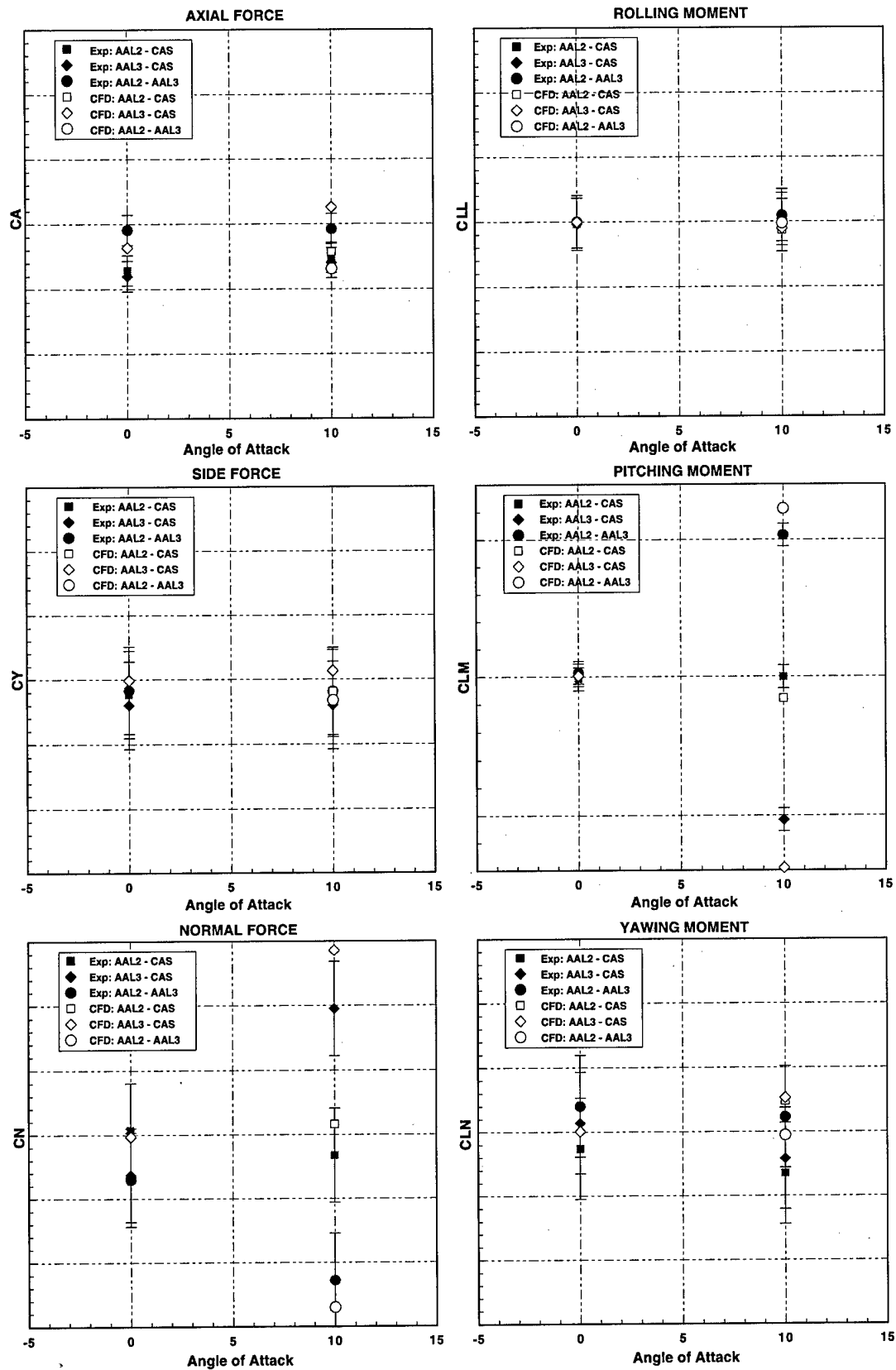


Fig. 16. Calculated increments; 0.9 Mach, 0 deg  $\beta$ .

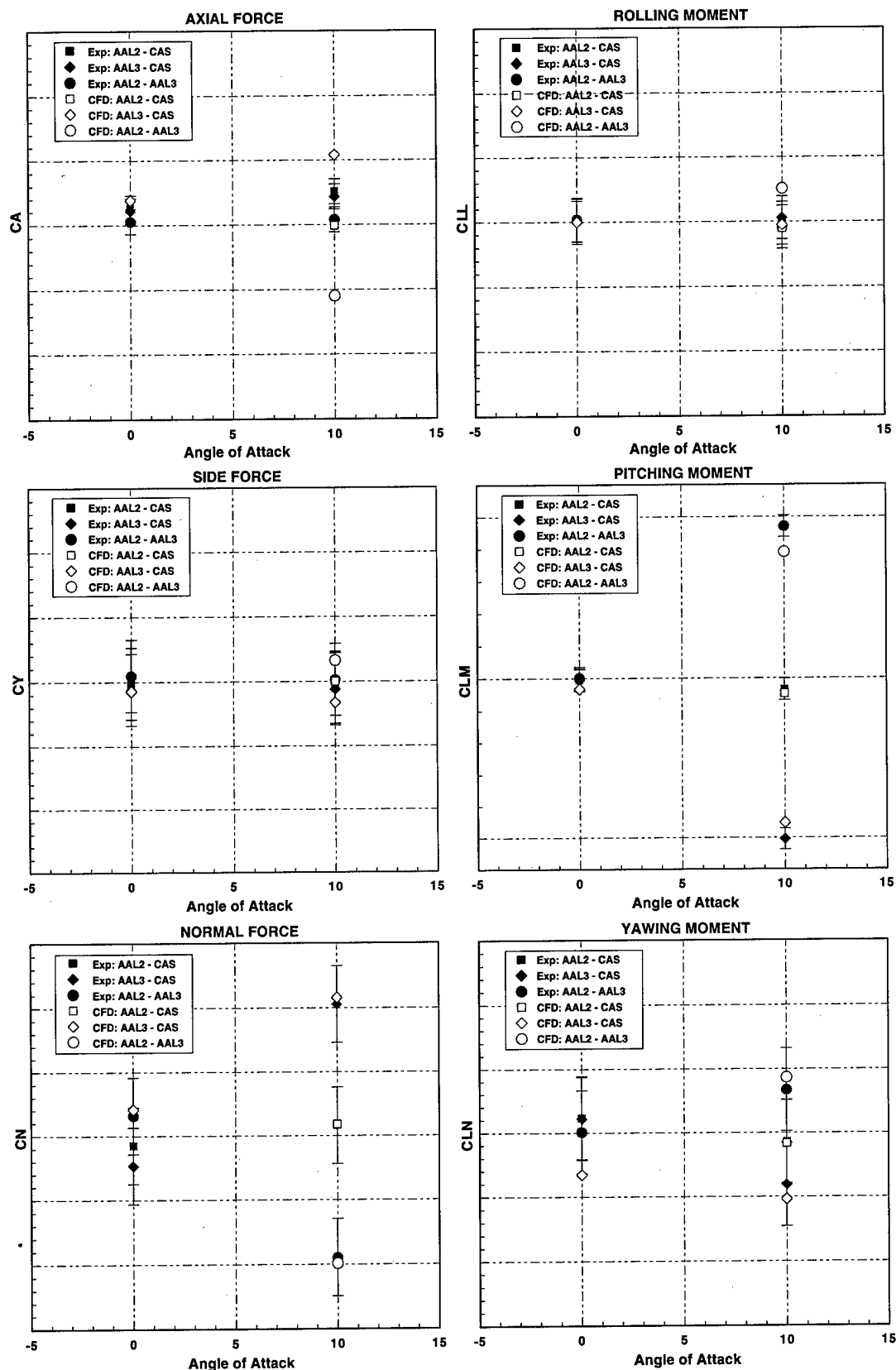


Fig. 17. Calculated increments; 1.4 Mach, 0 deg  $\beta$ .



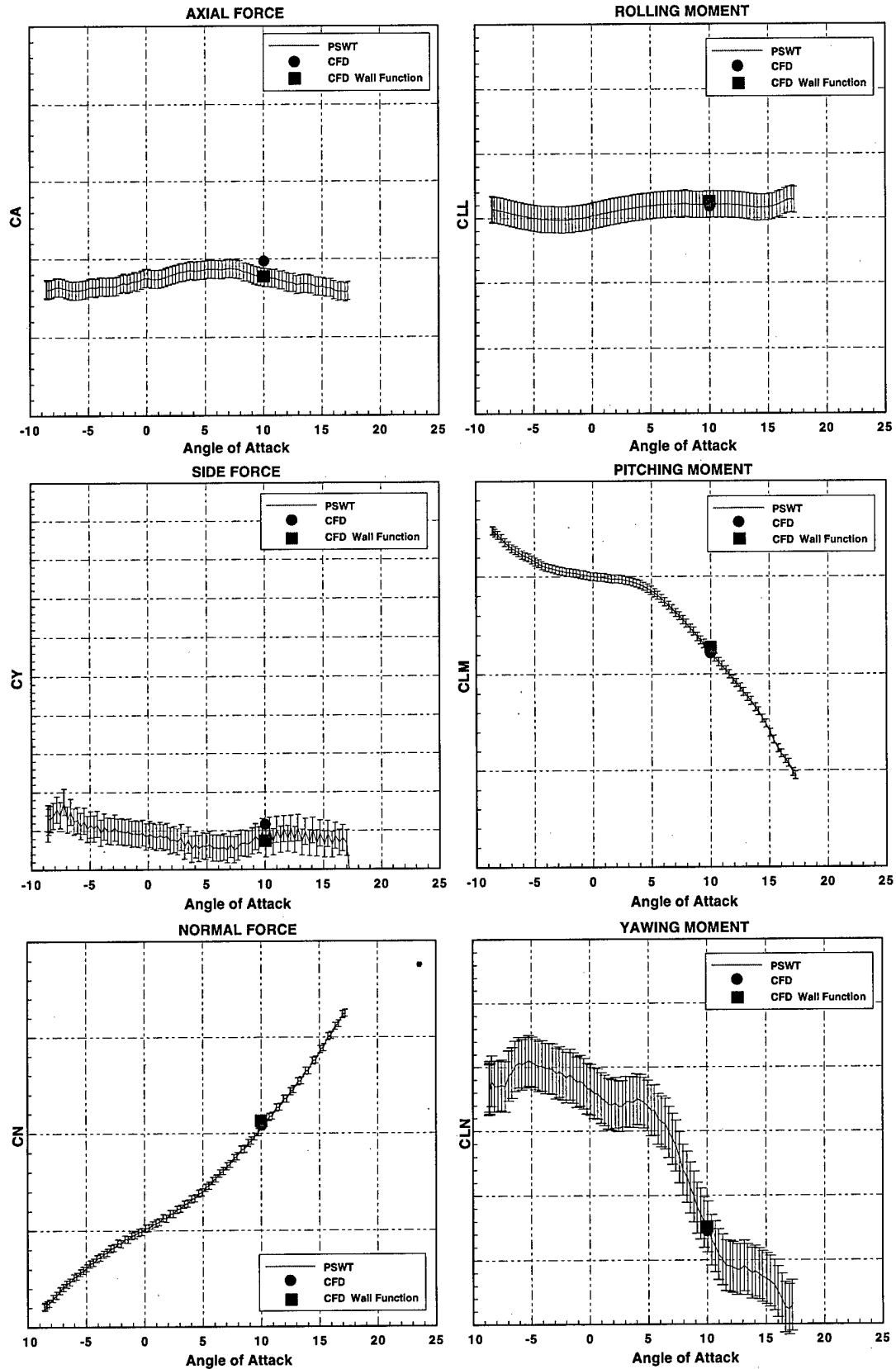


Fig. 18. Correct afterbody, small sting; 0.9 Mach, 5 deg  $\beta$ .

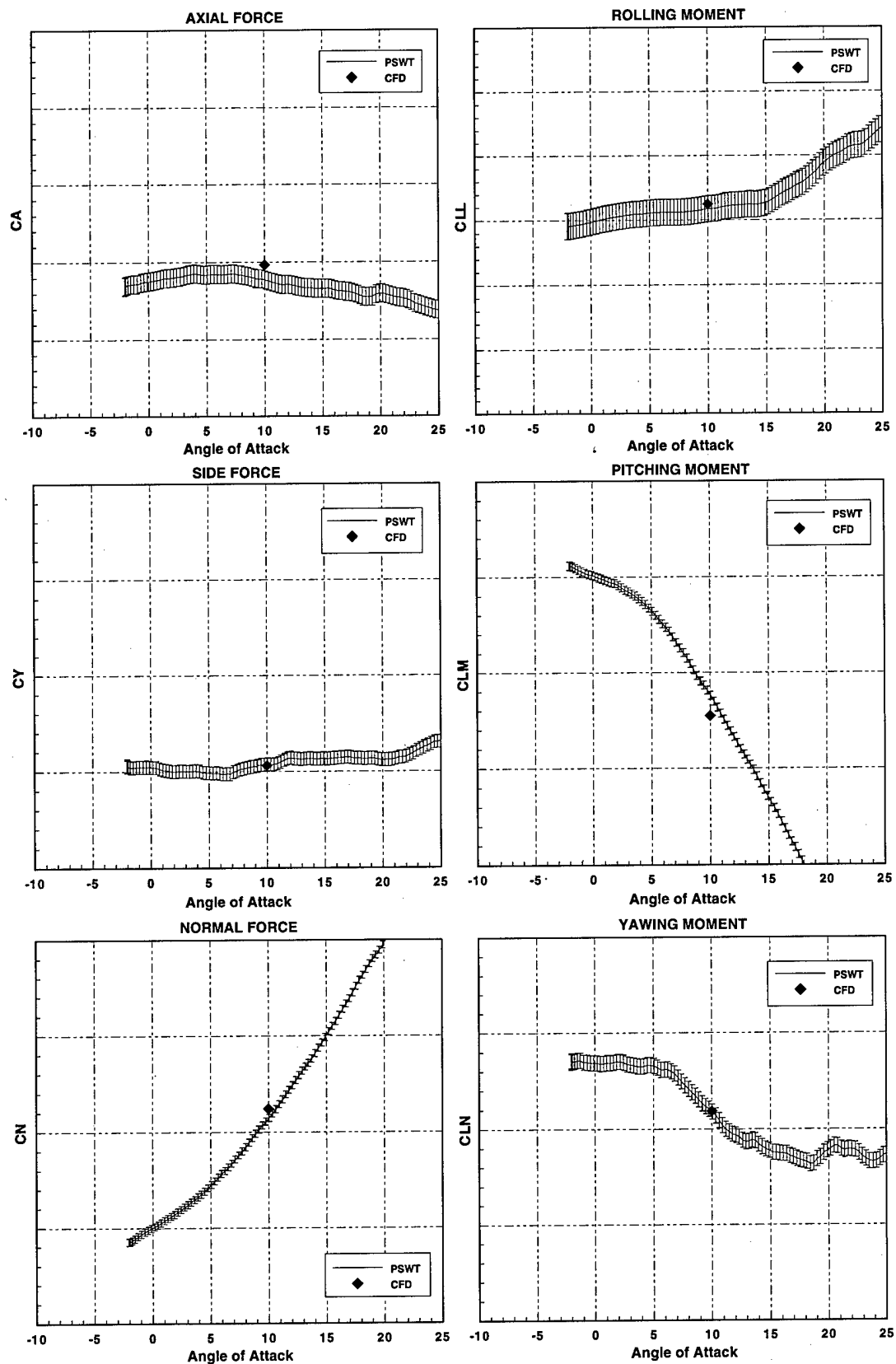


Fig. 19. Altered afterbody, large sting, area-matched fins; 0.9 Mach, 5 deg  $\beta$ .

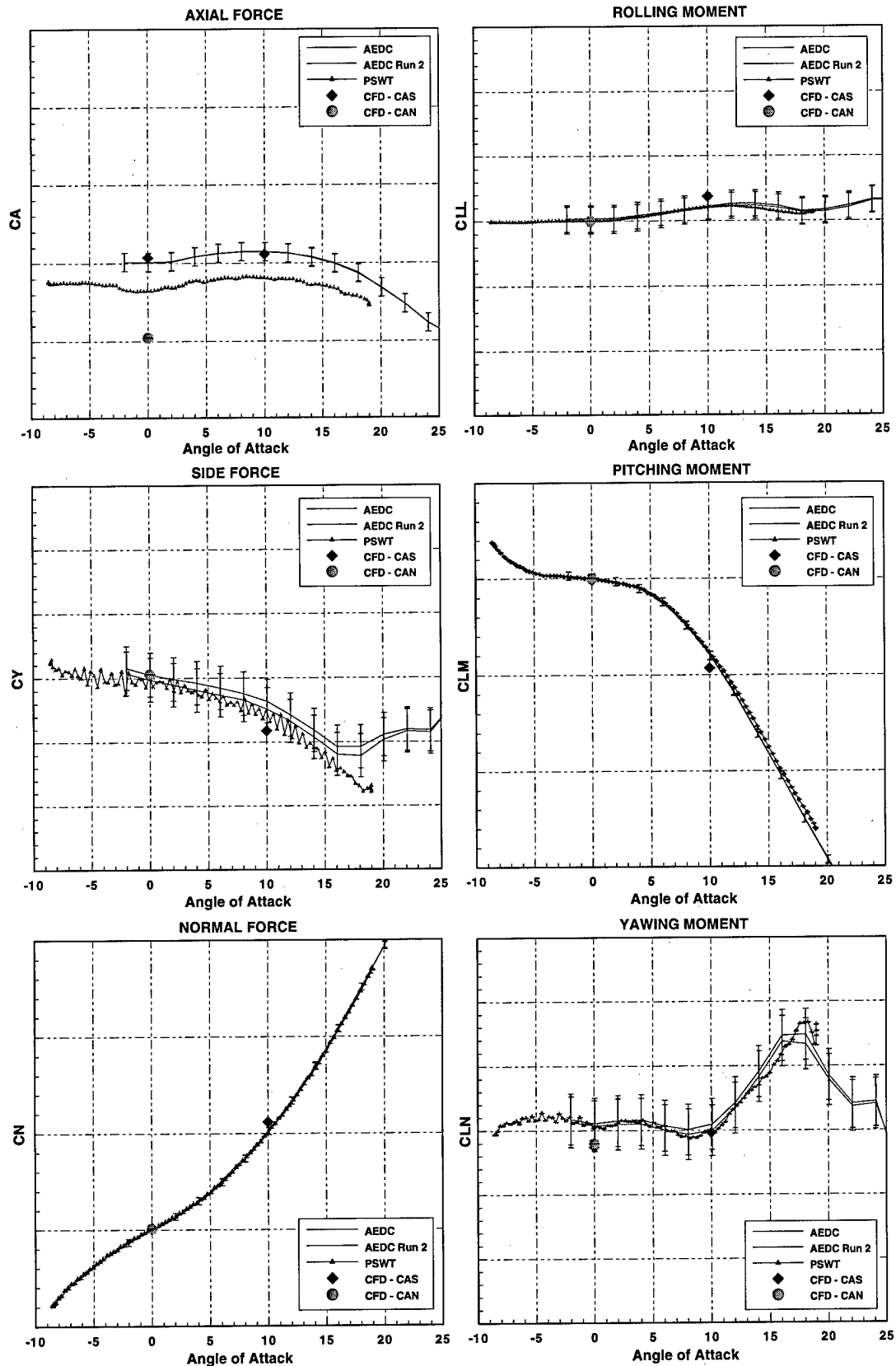


Fig. 20. Correct afterbody with and without sting; 0.9 Mach, 0 deg  $\beta$ .

## References

1. Whitby, D. G. "Wind Tunnel Support System Effects on a Fighter Aircraft Model at Mach Numbers from 0.6 to 2.0." AEDC-TR-89-4 (AD-A210614), July 1989.
2. Rist, M. J. "Computational Investigation of Wind Tunnel Support Interference." AIAA 94-2602.
3. Benek, J. A., Steger, J. L., Dougherty, F. C., and Buning, P. G. "Chimera: A Grid-Embedding Technique." AEDC-TR-85-64 (AD-A167466), December 1985.
4. Benek, J. A., Donegan, T. L., and Suhs, N. E. "Extended Chimera Grid Embedding Scheme with Application to Viscous Flows." AIAA 87-1126CP, June 1987.
5. Nichols, R. H., "Development and Validation of a Two-Equation Turbulence Model with Wall Functions for Compressible Flow." AIAA 96-2385, June 1996.
6. Suhs, N. E., Nichols, R. H., and Denny, A. G., "Unsteady Viscous Flow Computations Using a Two-Equation Turbulence Model with Wall Functions." AIAA 96-2430, July 1996.
7. Beam, R., and Warming, R. F., "An Implicit Finite-Difference Algorithm for Hyperbolic Systems in Conservation-Law Form." *Journal of Computational Physics*, Vol. 22, No.1, September 1976, pp. 87-110.
8. Baldwin, B. S. and Lomax, H. "Thin Layer Approximation and Algebraic Model for Separated Turbulent Flows." AIAA 78-257, January 1978.
9. Nichols, R. H. "A Two-Equation Model for Compressible Flows." AIAA 90-0494, January 1990.
10. Dietz, W. E. "General Approach to Calculating Forces and Moments on Overset Grid Configurations." Proceedings of the Second Overset Composite Grid and Solution Technology Symposium, October 1994.